POLISH MARITIME RESEARCH 1 (129) 2026 Vol. 33; pp. 74-90
10.2478/pomr-2026-0007

Numerical Simulation and Analysis of the Cavitation Noise Characteristics of an IMP Propulsor

Qiao Li [1, 2 *]
Shahrir Abdullah [1, 3]
Mohammad Rasidi Mohammad Rasani [4]

[1] Dept. of Mechanical and Manufacturing Engineering, Faculty of Engineering and Built Environment, UniversitiKebangsaan Malaysia, Bangi, Malaysia
[2] Department of Intelligent Manufacturing, Guangdong Technology College, Zhaoqing, China
[3] Centre for Automotive Research, Faculty of Engineering and Built Environment, UniversitiKebangsaan Malaysia, Bangi, Malaysia
[4] Dept. of Mechanical Engineering, Faculty of Engineering, Universiti Teknologi PETRONAS, Seri Iskandar, Perak, Malaysia

* Corresponding author: *p112282@siswa.ukm.edu.my (Qiao Li)*

ABSTRACT

The objective of this study is to ascertain the cavitation noise characteristics of an integrated motor pump-jet (IMP) propulsor. The far-field cavitation radiation noise of the propulsor is analysed using computational fluid dynamics and acoustic coupling methods. The results indicate that in comparison with non-cavitation noise, the IMP propulsor generates an increased level of noise as a consequence of cavitation. Strong correlation is observed between the variables of cavitation volume pulsation and radiation noise. The initial rise in the overall sound pressure level of the radiation noise inside the propulsor is followed by a gradual increase as the degree of cavitation deepens. Concurrently, the total noise increases, while the significance of the blade frequency weakens. Variations in the blade tip gap have a pronounced influence on the intensity of cavitation noise. Under identical conditions in terms of the axial gap, the cavitation noise attains its minimum level when the radial gap is set to 3 mm. Conversely, an increase in the axial gap results in a corresponding rise in cavitation noise when the radial gap remains constant. The findings of this study will provide valuable insights for the noise control of IMP propulsors.

Keywords: IMP propulsor; cavitation; radiated noise; sound pressure level; numerical simulation

INTRODUCTION

In recent years, there has been an increased level of interest in the integrated motor pump-jet (IMP) propulsor, primarily due to its adaptability, reliability, and low space occupancy requirements. IMP propulsor systems have typically been used in high-performance underwater vehicles, such as submarines and torpedoes. The acoustic performance of these technologies directly influences the stealth capabilities of a submersible [1], meaning that research into the noise characteristics of IMP propulsor systems is of significant value.

The internal flow of an IMP propulsor can be classified into two types: (i) flow noise caused by turbulent pulsations and disturbances, such as cavitation bubble collapse, and (ii) structurally induced noise caused by increased structural vibration due to excitation forces [2]. At high speeds, the principal sources of noise in an IMP propulsor system are the rotor load and thickness noise, and the vortex shedding noise [1]. This type of noise has sophisticated coupling features, making it an important area of focus and a difficult problem in the field of IMP propulsor noise research.

Du et al. [3] studied the noise radiation characteristics of a rear stator pump-jet propulsor and found that rotor noise in the axial direction had the greatest impact, while duct noise in the small-scale radial direction also had a considerable impact on the overall noise. Sun et al. [4] adopted a method based on

computational fluid dynamics (CFD) and an aeroacoustics analogy to calculate the noise sources and far-field noise for each component of the pump-jet. Liu et al. [5] applied Lighthill's acoustic analogy theory and a hybrid numerical simulation method to analyse the influence of flow variation on the frequency domain characteristics of the sound pressure level (SPL) and overall sound pressure level (OSPL) of flow-induced noise in a shaftless pump-jet propulsor and its relationship with the internal flow field. After verifying the reliability of surface noise prediction from external sound sources, Qin et al. [6] carried out noise prediction for a pump-jet propulsion system. Their approach was based on an improved method of delayed detached eddy simulation and Ffowcs Williams-Hawking (FW-H) acoustic analogy. The results demonstrated that within 500 Hz, the broadband sound pressure level obtained by overlapping the sound fields of each individual component exhibited strong agreement with the results obtained from the overall calculation [7]. Ianniello et al. [8] assessed underwater noise from non-cavitating marine propellers in uniform flow, and highlighted the impact of nonlinear noise sources such as turbulence and vorticity. Nitzkorski and Mahesh [9] enhanced the accuracy of their simulations by implementing a dynamic end cap technique with the FW-H equations. Mathey [10] suggested a hybrid technique that combined the Reynolds-averaged Navier–Stokes equations with large eddy simulation, and used the FW-H equation to determine the far-field noise at the interface of these two methods. These engineering applications demonstrate the accuracy of the FW-H equation and provide a rationale for computing propeller noise.

Although flow-induced noise has been extensively studied, research on reducing cavitation noise to improve the acoustic stealth of submarines is limited. McCormick et al. [11] studied experimental data on propeller cavitation flow noise and found that pump-jet propellers outperformed standard propellers in terms of efficiency, noise, and cavitation performance. Testa et al. [12] used a boundary element equation founded upon the velocity potential to resolve the fluctuating pressure on the propeller surface in the context of cavitation. In order to examine the cavitation noise characteristics of centrifugal pumps, Si et al. [13] applied a constructed numerical method for cavitation noise in order to solve the acoustic field, based on the flow field solutions. A comparison of results from experiments and simulation revealed to be consistent and reliable. In a study by Wei et al. [14], the acoustic behaviour of hydrofoils in a cavitation state was predicted and analysed based on the FW-H acoustic analogy method. Sakamoto and Kamiirisa [15] did not use the FW-H acoustic analogy method; instead, they predicted the near-field propeller cavitation-induced noise based on a viscous CFD semi-empirical method. The effectiveness of this method was verified by comparing it with experimental data. Jeong et al. [16] simulated the initial noise generated by cavitation in a tip vortex and studied the initial cavitation velocity under different flow conditions. In their study, Ku et al. [17] examined the occurrence of cavitation-induced noise at the tip of a vortex under varying water quality conditions. Their predictions regarding sound pressure levels had a high degree of congruence with the outcomes of experimental investigations. Park et al. [18] conducted experimental studies on cavitation noise from a propeller in a cavitation water tunnel under non-uniform flow conditions, and attempted to locate the sound sources in the flow field. Pennings et al. [19] conducted experimental measurements of propeller cavitation noise using a specially designed double-blade propeller. Bosschers [20] proposed a semi-empirical prediction method for underwater radiation noise caused by ship propellers, which was based on the three main modes of vortex cavitation. The influence of changes in the vortex cavitation shape parameters over time on the pressure pulsations was analysed, and satisfactory prediction results were achieved.

Since studies of noise have rarely involved IMP propulsion, this article presents research on cavitation noise. In order to verify the accuracy of the noise calculation method, the load noise for the E779A propeller is calculated and the results are compared with those from the relevant literature. The detached eddy simulation (DES) and Zwart-Gerber-Belamri (ZGB) cavitation models are then used to simulate the IMP propulsor's flow field. The sound field is resolved using the flow field solutions and the current cavitation noise numerical calculation method. In order to facilitate a more thorough examination of the factors impacting cavitation and noise in the future, the cavitation flow is also calculated for different gaps. This enables a more thorough comparison and study of the law governing this change, as well as a more detailed analysis of the far-field noise characteristics under each operating condition. The purpose of this study is to provide a reference for noise reduction design and research into the noise characteristics of IMP propulsors.

RESEARCH OBJECT AND COMPUTATIONAL MODEL

GEOMETRICAL MODEL AND COMPUTATIONAL DOMAIN

This study focuses on the IMP propulsor, which was self-developed [21]. The rotor blades of the IMP propulsor are based on the NACA 4409 airfoil, while the guide vanes are based on the 443 airfoil. The No. 19A duct is adopted to accommodate the installation of the motor. The IMP propulsor calculation model is illustrated in Fig. 1, and the main parameters of the propulsor are calculated from the matching points, as shown in Table 1.

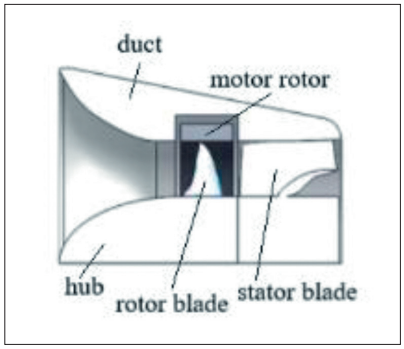

Fig. 1. Model of the IMP propulsor (due to the symmetry of the structure, only one quarter of it is considered)

Tab. 1. Main parameters of the propulsor

Nozzle diameter (*mm*)	601
Flow rate of propulsor pump (m^3/s)	1.48
Ratio speed	295
Rotational speed (*r/min*)	780
Propulsor pump head (*m*)	0.84
Cavitation ratio speed	139.34
Thrust (*N*)	2250.21
Thrust efficiency	0.95

The computational domain is divided into three components, which are formulated based on the physical challenges addressed in this study. These components are the external flow field, the rotor system, and the stator subsystem. The rotor and stator systems are embedded in an external flow field, with the rotor system constituting the rotating domain and the stator system representing the static domain. A sliding mesh technique is employed to simulate the interaction between the two regions. In this study, a cylindrical region coaxial with the pump-jet is considered as the calculation domain, with the aim of enhancing the realism of the numerical calculation, as illustrated in Fig. 2. The maximum diameter of the IMP rotor is designated as D. The inlet and outlet boundaries of the computational domain of the external flow field are positioned at distances of 3D and 6D from the rotor, respectively, and the diameter of the external flow field is 6D.

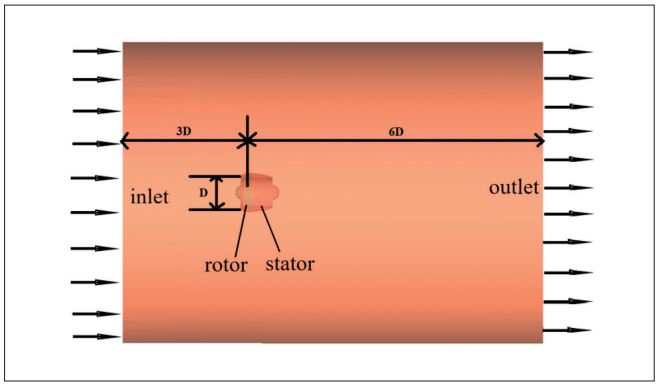

Fig. 2. Computational domain

The IMP propulsor consists of several structural components, including an impeller blade and a guiding vane with a body-fitted grid. The remaining sub-blocks are divided by a structural grid and then connected to the overall grid system. For grid coupling, the grid at the sub-block interface must be both smooth and continuous. Fig. 3 shows the grid for each block, and Fig. 4 depicts the overall grid for the computing area. A total of 3,605,181 grid nodes were created across the domain.

The axial and radial gaps of the IMP propulsor need to be given due consideration during the gridding process. The air gap range can be processed using a structured grid by implementing a grid in which the initial layer of the air-gap wall is measured as 0.008 mm in thickness, with a subsequent relative augmentation of 120% in the thickness of each subsequent layer of the grid (refer to Fig. 5). The maximum y+ value of the pump-jet wall is 45.8, which meets the requirements of the turbulence model.

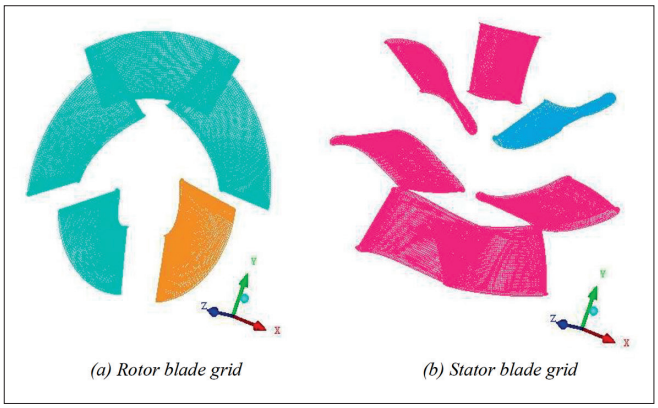

(a) Rotor blade grid *(b) Stator blade grid*

Fig. 3. Spatial blocking grids

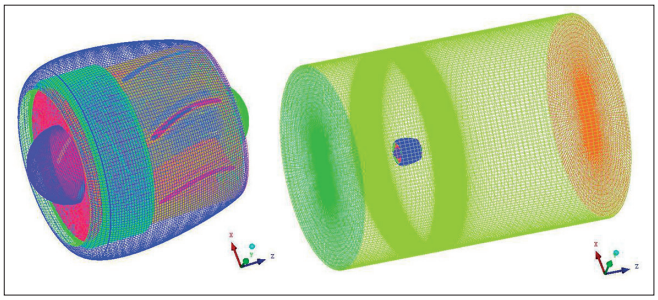

Fig. 4. Overall grid for the calculation area

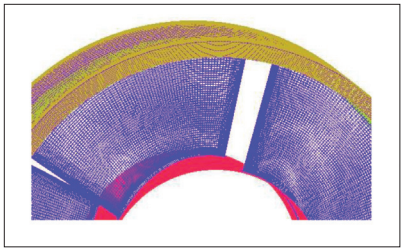

Fig. 5. Magnified grid for the rotor and air-gap wall surface

To ensure the correctness and accuracy of the grid, independent verification was required. By increasing the number of boundary layer nodes, five sets of grids were obtained, with 1.76 million, 3.6 million, 4.9 million, 6.5 million, and 8.9 million cells. Under design conditions, we compared the thrust coefficient, torque coefficient, and propulsion efficiency for computational domains with different numbers of cells to determine the most suitable grid size, as shown in Table 2. It can be seen from the table that the fluctuation in propulsion efficiency becomes insignificant and stabilises as the number of grid nodes increases. As a result, taking into account both the computing efficiency and consumption of computational resources, a total of 3,605,181 grid nodes was chosen for the numerical analysis.

Tab. 2. Grid-independent verification

J	Number of grid nodes	K_T	K_Q	η
1.02	1 768 631	0.119	0.036	53.66%
	3 605 181	0.120	0.035	56.69%
	4 903 435	0.121	0.035	56.54%
	6 501 002	0.119	0.036	56.51%
	8 902 530	0.120	0.036	56.46%

The boundary conditions included the velocity at the inlet and the pressure at the outlet, with an operating pressure of

zero. Different cavitation numbers were achieved by adjusting the outlet pressure. No-slip wall conditions were imposed on the rotor blades, stator blades, hub, and duct. A free-slip wall was imposed on the side surface of the cylindrical domain. The bubble volume fraction was set to zero at the inlet, while the liquid volume was set to 1%, and the turbulence intensity was set to its default value. The pressure at the outlet boundary was controlled by the cavitation number $\sigma = p_{out} - p_v/0.5\rho_l v^2$, where p_{out} is the outlet pressure, and v is the incoming velocity. The physical parameters of the fluid flow field were a liquid temperature of 25°C, a liquid saturation vapor pressure of 3,540 Pa, and densities for the liquid and gas of 1000 kg/m^3 and 25.28 g/m^3, respectively.

DES was employed in this study to capture the large-scale unsteady turbulent structures. The DES formulation is based on the SST k–ω model, in which the turbulence length scale is $l_{DES} = min(\frac{\sqrt{k}}{\omega}, C_{DES}\Delta)$, where $C_{DES} = 0.65$ and Δ denotes the local grid spacing.

The convective terms were discretised using a first-order upwind scheme, while a first-order implicit scheme was employed for time integration. The pressure–velocity coupling was handled using the SIMPLEC algorithm. Convergence was achieved when all residuals dropped below 10^{-5}, and the monitored thrust and torque reached a statistically steady state.

Unsteady CFD simulations were performed using the SST k–ω turbulence model coupled with the ZGB cavitation model. A time-step sensitivity study was conducted to evaluate the influence of the temporal resolution on the numerical results: three-time steps of 0.28, 0.14, and 0.07 ms, corresponding to approximately 37, 75, and 150 time steps per blade passing period, respectively, were considered while all other parameters were unchanged.

The thrust coefficient was selected as a representative quantity for comparison. The relative difference between the medium and fine time steps was less than 1%, indicating that further time-step refinement had a negligible effect on the results. A time step of 0.14 ms was therefore adopted for all subsequent simulations as a compromise between numerical accuracy and computational efficiency.

ACOUSTIC SIMULATION THEORY OF CAVITATION AND ACOUSTIC SETTINGS

Acoustic simulation theory of cavitation

In this study, the impact of non-condensable gas (NCG) was incorporated into the cavitation model, and the ZGB cavitation model was used to calculate the speed at which the gas entered the liquid phase. The ZGB cavitation model assumes that all bubbles in the system have the same initial diameter. To calculate how quickly the mass of a single bubble changes, we can use the following formula:

$$\frac{dm_B}{dt} = \rho_v \frac{dV_B}{dt} = 4\pi R_B^2 \rho_v \sqrt{\frac{2}{3}\frac{p_v - p}{\rho_l}} \tag{1}$$

The vapour volume fraction is:

$$\alpha_v = N_B V_B = \frac{4}{3}\pi R_B^2 N_B \tag{2}$$

where m_B is the mass of the bubble, V_B is the volume of the bubble, ρ_v is the gas phase density, ρ_l is the liquid density, p_v is the evaporation pressure of the liquid at the local temperature, p is the liquid pressure around the bubble, α_v is the volume fraction of the gas phase, N_B is the number of bubbles per unit volume, and R_B is the radius of the bubble.

The total mass transfer rate is:

$$m_t = N_B \frac{dm_B}{dt} = \frac{3\alpha_v \rho_v}{R_B} \sqrt{\frac{2}{3}\frac{p_v - p}{\rho_l}} \tag{3}$$

Eq. (4) describes the generation and collapse of cavitation:

$$R_e = F \frac{3\alpha_v \rho_v}{R_B} \sqrt{\frac{2}{3}\frac{|p_v - p|}{\rho_l}}\, sign(p_v - p) \tag{4}$$

where R_e is the vapor production rate. The ZGB cavitation model can be formulated by replacing α_v with $\alpha_{NCG}(1-\alpha_v)$:

$$m_t = -F_{vap} \frac{3\alpha_{NCG}(1-\alpha_v)\rho_v}{R_B} \sqrt{\frac{2}{3}\frac{p_v - p}{\rho_l}}\ ,\ p \le p_v \tag{5}$$

$$m_t = F_{cond} \frac{3\alpha_v(1-\alpha_v)\rho_v}{R_B} \sqrt{\frac{2}{3}\frac{p_v - p}{\rho_l}}\ ,\ p > p_v \tag{6}$$

where $\alpha_{NCG} = 5 \times 10^{-4}$ is the NCG volume fraction, $F_{vap} = 50$ is the empirical coefficient of bubble generation, and $F_{cond} = 0.001$ is the empirical coefficient of bubble coagulation.

The monopole noise source associated with the cavitation volume in the flow field can be calculated with spherical cavitation radiation theory. A brief overview of this hypothesis is as follows [22,23]. We consider cavitation to be a simple pulsation source and assume that the diameter of the cavitation bubble is significantly lower than the typical wavelength. In this situation, the cavitation bubble can be considered a point pulsation source, and the sound pressure at a monitoring point away from the centre of the sphere is:

$$p'(r, t) = \frac{\dot{Q}(t)}{4\pi r} \tag{7}$$

$$Q = \int q dV = \frac{d}{dt}(\rho_l V) \tag{8}$$

where ρ_l is the fluid density, kg/m^3; r is the observation distance, m; and V is the volume of the cavitation bubble, m^3.

If the compressibility of the fluid is not considered, Eq. (7) can be expressed as:

$$p'(r, t) = \frac{\rho_l}{4\pi r}\left(\ddot{V}(t)\right) \tag{9}$$

Eq. (9) can be used to compute the sound pressure produced by the noise emitted by a single bubble. This equation shows that the sound pressure is directly related to the volume acceleration of the cavitation bubble. In realistic cavitation settings, the noise produced by the volume pulsation of several randomly forming bubbles adds to the overall acoustic output. To adequately account for volume pulsation in cavitation bubbles, an analogous volume source is developed, in which the actual surfaces are represented as the virtual surface of a spherical bubble. A suitable choice of far-field sound pressure monitoring stations allows the sound pressure fluctuations caused by pulsation of the cavitation bubble volume to be calculated.

Acoustic settings

The FW-H method is used to calculate the radiation noise of the pump-jet propulsion system, with the model wall surface acting as the sound source [24,25]. The noise data are obtained by analysing the transient pressure pulsations on the wall surface.

The equations for the FW-H acoustic analogy are:

$$\frac{1}{c_\infty^2}\frac{\partial^2 p'}{\partial t^2} - \nabla^2 p' = \frac{\partial}{\partial t}\left\{\left[\rho_\infty v_n + \rho(u_n - v_n)\delta(f)\right]\right\} - \frac{\partial}{\partial x_i}\left\{\left[\rho_{ij} v_j + \rho u_i (u_n - v_n)\delta(f)\right]\right\} + \frac{\partial^2}{\partial x_i \partial y_j}\left\{T_{ij} H(f)\right\} \quad (10)$$

$$T_{ij} = \rho u_i u_j + \sigma_{ij} - c^2(\rho - \rho_\infty)\delta_{ij} \quad (11)$$

$$\sigma_{ij} = -p\delta_{ij} + \mu\left(\frac{\partial u_i}{\partial x_j} + \frac{\partial u_j}{\partial x_i} - \frac{2}{3}\frac{\partial u_k}{\partial x_k}\delta_{ij}\right) \quad (12)$$

where u_i and v_i are the components of fluid velocity and surface velocity in the x_i direction, respectively; u_n and v_n are the components of fluid velocity and surface velocity in the direction normal to the surface ($f = 0$), respectively; $\delta(f)$ represents the Dirac delta function; and $H(f)$ represents the Heaviside function.

The three terms on the right-hand side of Eq. (10) represent the acoustic source terms of a non-uniform monopole, a dipole and a quadrupole, respectively. The monopole source represents noise generated by fluid mass fluctuations caused by a moving surface, whereas the dipole source corresponds to noise generated by surface wave dynamics on a body's surface, and the quadrupole source represents noise generated by fluid wave stresses outside the body. The full solution is expressed using surface and volume integrals: the surface integral accounts for the monopole and dipole sound sources, while the volume integral represents the quadrupole sound source outside the source surface. For flow velocities with low Mach numbers, the contribution of the volume integral can be neglected. After removing the volume integral, the analytical solution to Eq. (10) can be obtained as follows:

$$p'(x, t) = p'_T(x, t) + p'_L(x, t) \quad (13)$$

$$4\pi p'_T(x, t) = \int_{f=0}\left[\frac{\rho_\infty(\dot{U}_n + U_i)}{r(1-M_r)^2}\right]_{ret} dS + \int_{f=0}\left[\frac{\rho_\infty U_n\{rU_r + c_\infty(M_r - M^2)\}}{r(1-M_r)^3}\right]_{ret} dS \quad (14)$$

$$4\pi p'_L(x, t) = \frac{1}{c_\infty}\int_{f=0}\left[\frac{\dot{L}_r}{r(1-M_r)^2}\right]_{ret} dS + \int_{f=0}\left[\frac{L_r - L_M}{r^2(1-M_r)^2}\right]_{ret} dS + \frac{1}{c_\infty}\int_{f=0}\left[\frac{L_r\{M_r + c_\infty(\dot{M}_r - M^2)\}}{r^2(1-M_r)^3}\right]_{ret} dS \quad (15)$$

where the subscript *ret* indicates the delay time calculation integral when the sound is emitted; t is the monitoring time; r is the distance between the sound source and the monitoring point; and M_r is the local Mach number.

COMPUTATION AND VALIDATION OF PROPELLER NOISE

NUMERICAL CAVITATION SIMULATION AND VALIDATION OF THE TRANSIENT FLOW FIELD FOR THE PROPELLER

To verify the accuracy of the numerical method developed in this paper, a four-bladed E779A propeller was selected as a computational model. The cavitation performance was numerically simulated using the aforementioned numerical approach, based on the modified SST k–ω turbulence model and the ZGB cavitation model. The numerical method for cavitation prediction was validated by analysing and comparing the simulation results.

The main parameters of the E779A propeller are listed in Table 3. Based on the characteristics of the numerical simulations, the computational domain was divided into two parts: the E779A propeller domain, and the outer flow field domain. The propeller domain was set as a rotating reference frame, whereas the outer flow field domain was kept stationary. For the steady-state calculations, we assume that the distributions of the flow quantities, such as pressure and velocity, are identical for each blade, as the computational domain exhibits rotational periodicity. A periodic boundary condition was therefore applied to simulate a single flow passage of the E779A propeller. As shown in Fig. 6, the entire E779A propeller domain was modelled as a quarter-cylinder, with an axis coinciding with that of the propeller and a diameter of $5D_1$ (where D_1 is the diameter of the E779A propeller). The inlet boundary of the computational domain was located $6D_1$ upstream from the front end of the propeller domain, and the outlet boundary was located $10D_1$ downstream from the rear end of the propeller domain. The entire computational domain consisted of 439,902 structured grid nodes, 305,796 of which belonged to the E779A propeller domain.

Tab. 3. Main parameters of the E779A propeller

Propeller diameter (D_1)	Pitch ratio (P/D_1)	Rake angle	Skew angle	Expanded area ratio	Hub diameter (D_H)
227.3 *mm*	1.1	4°48″	4°3″	0.689	45.53 *mm*

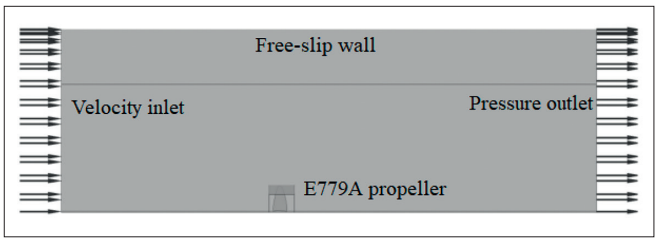

Fig. 6. Computational domain and boundary conditions of the E779A propeller

Three turbulence models were employed to analyse the power of the E779A propeller at different rotational speeds of the rotor. The results were compared with measured values provided by the KaMeWa Corporation, as shown in Table 4. The results indicate that the outcomes from all three models are lower than

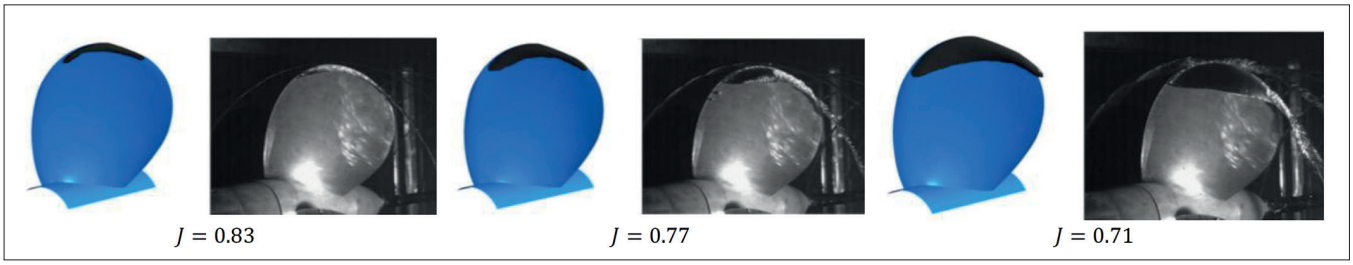

Fig. 7. Comparison of cavitation areas on E779A propeller blades with experimental photographs at different values of the advance coefficient

the measured values. The measured values showed the closest agreement with the SST k–ω model, with the smallest error; this is because the SST k–ω model combines the advantages of both the realisable k–ε model and the standard k–ε model, and offers computational advantages in near-wall regions. To better capture the cavitation patterns on the surfaces of the impeller and guide vane blades, the SST k–ω model was selected as the turbulence model for this study. The results demonstrate the suitability of this model and the reliability of the numerical simulation method.

Tab. 4. Numerical simulation of the power of the mix-flow pumps compared with the values provided by the company

n/ r /min	SST k–ω error /%	Realisable k–ε error /%	Standard k–ε error /%	Manufacturer-provided value /kW
500	–0.59	–1.19	–2.38	457
700	–0.79	–1.72	–1.98	1205
900	–0.70	–1.29	–1.99	2507
1100	–0.84	–0.74	–1.12	4375
1300	–1.08	–1.39	–1.39	7098

A numerical simulation of the cavitation performance of the E779A propeller was conducted using the same fluid physical properties and cavitation simulation settings as those applied to the NACA66 hydrofoil. Steady-state cavitation performance simulations were carried out for the E779A propeller at three representative advance coefficients (J = 0.71, 0.77 and 0.83), and the results were compared with experimental data. Fig. 7 shows a comparison between the simulated results for the cavitation area on the propeller blades at three typical cavitation numbers and the corresponding experimental observations. It can be seen that cavitation initially occurs at the tip region on the pressure side of the propeller blades. As the advance coefficient increases, the cavitation phenomenon becomes more pronounced, and the region expands progressively from the blade tips over the entire blade surface. A comparison of the numerical predictions with experimental photographs shows good agreement in terms of the location, shape and extent of the cavitation region; however, slight discrepancies are observed in the tip-vortex cavitation at lower advance coefficients, which may be attributed to differences in the grid quality and modelling accuracy in the blade-tip region.

Fig. 8 shows efficiency curves for the E779A propeller at various cavitation numbers. Once the cavitation number exceeds 2.2, the propeller's efficiency shows no significant variation, and the numerical predictions are closely aligned with the experimental results. When the cavitation number exceeds a critical threshold, cavitation on the blade surface disappears entirely; as a result, the propulsive efficiency becomes insensitive to σ and approaches a constant level. A comparison of the efficiency curves at two advance coefficients reveals that the lower the advance coefficient, the more sensitive the efficiency to changes in cavitation. More specifically, when J = 0.83, the variation in the efficiency curve with increasing cavitation number is less pronounced than at J = 0.71. This is mostly due to the fact that with lower advance coefficients, the propeller runs at a faster rotational speed or under a heavier load. This leads to increased cavitation intensity, which has a stronger impact on hydrodynamic performance. As a result, the efficiency at lower advance coefficients is more susceptible to changes in the cavitation number. This analysis provides further support for the suitability of the model and the reliability of the numerical simulation method used here.

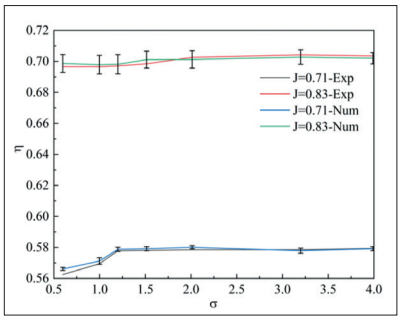

Fig. 8. Efficiency curves of the E779A propeller under different cavitation numbers

NUMERICAL SIMULATION AND VALIDATION OF PROPELLER LOADING NOISE

To validate the load noise of the E779A propeller, calculations were performed based on the results of the stable transient flow field. These transient flow field and load noise calculations were conducted at a design pitch speed of J = 0.83 and an incoming flow velocity of 8.395 m/s, corresponding to a propeller rotational speed of 41.975 r/s. Fig. 9 presents a diagram showing the layout of the noise monitoring points.

Finally, the FW-H model was set up to perform far-field sound field calculations. The results for the time-domain load component of sound pressure at the monitoring point were subjected to a fast Fourier transform (FFT) to obtain the frequency-domain load component of sound pressure for the single blade. These single-blade load noise values were then compared with the values in reference [26] (see Fig. 10). The results are in good agreement with those in the literature for the shaft frequency (42 Hz), the blade passing frequency (168 Hz)

and their harmonics. This demonstrates the reliability of the FW-H model-based method for calculating far-field noise.

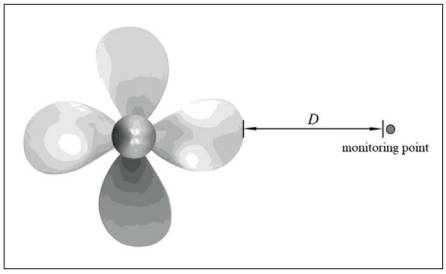

Fig. 9. Location of the noise monitoring point for the E779A propeller

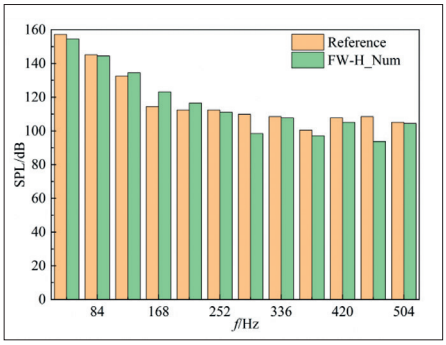

Fig. 10. Calculated values and comparison of single-blade load noise

COMPUTATION AND ANALYSIS OF IMP PROPULSOR NOISE

TRANSIENT FLOW FIELD COMPUTATION OF THE IMP PROPULSOR

Transient flow field calculations were performed using the steady-state calculation results as initial values, with the corresponding IMP propulsor speed set to 19.17 r/s. For these transient flow field calculations, the DES model was employed, with the calculation time step set to 0.14 ms, corresponding to the time taken for the rotor to rotate through 1°. Before calculating the transient flow field, five pulsating pressure monitoring points were set up inside the IMP propulsor to analyse the internal flow characteristics, as shown in Fig. 11. Points A1 to A2 were located on the inlet and outlet surfaces of the rotor, distributed along the axial direction, whereas P1 to P3 were located at the blade tip gap of the rotor, with P1 near the leading edge of the rotor and P3 near the trailing edge. Following 12 rotational cycles of transient flow field calculation, the pulsating pressure monitoring results from the last two rotational cycles were analysed.

The power spectral density (PSD) of the pulsation pressure is a key parameter in noise analysis, as it directly characterises the energy intensity of the pulsation pressure distributed across the frequency spectrum on the rotor blade surface and surrounding flow field. The pulsation pressure is one of the sound sources for propulsor noise, and the peak and distribution of the PSD determine the main frequency and energy concentration zone of the noise, as can be seen in Figs. 12 and 13.

Figs. 12(a) and (b) show the characteristics of the pulsation pressure PSD at monitoring points A1–A2 along the radial

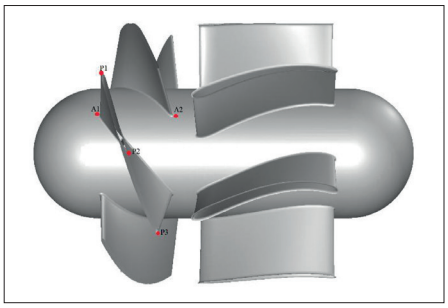

Fig. 11. Placement of monitoring points for the unsteady pressure inside the IMP propulsor

distribution on the rotor inlet surface and P1–P3 along the distribution from the leading edge to the trailing edge at the rotor blade tip gap. From Fig. 12(a), it can be seen that the PSD at A2 is generally higher than at A1. In front of the rotor, the pulsation pressure field is primarily dominated by the incoming turbulent flow, tip leakage vortices, and the rotor blade passing frequency (BPF) component, with the power spectrum typically exhibiting characteristic peak distributions centred around the BPF and its harmonics. After passing through the rotor, the flow structure is significantly modulated by factors such as the wake of the blade grid, the flow through the blade tip gap, and the potential initiation of cavitation in the suction or tip region of the blade, resulting in a redistribution of pulsation pressure energy in the frequency domain. This technique usually produces more energy in the low-frequency band and broadband increases in the mid-to-high-frequency bands. Fig. 12(b) shows that the pulsating pressure PSD at the leading and trailing edge positions of the rotor blades has significant spatial distribution differences, which are primarily due to differences in the characteristics of the incident flow field, vortex generation and evolution processes, and rotor–stator interaction mechanisms. Overall, the PSD shows a tendency towards peak shift, spectral broadening, and increased total energy along the chord from the leading to the trailing edge.

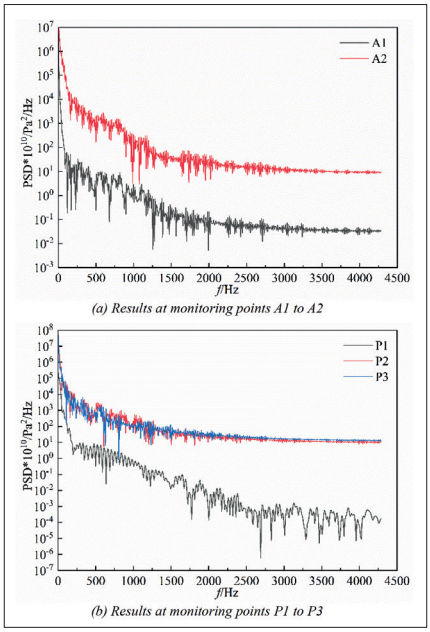

Fig. 12. Pulsation pressure PSD characteristics of the internal flow for the IMP propulsor

As illustrated in Fig. 13, the frequency domain plots were obtained by applying an FFT to the pulsation pressure results from each monitoring point in the time domain. Fig. 13(a) shows that the pressure pulsation magnitudes at the inlet and outlet surfaces A1 and A2 of the rotor both manifest at the first shaft frequency f_s (19.17 Hz) and its harmonics, with the peaks in pulsation pressure at the harmonics exhibiting significant attenuation. The dominant shaft frequency reflects the quasi-periodic nature of the rotor-induced pressure field, whereas the decay in harmonic amplitudes implies reduced acoustic efficiency at higher frequencies, a finding that is consistent with weakening coherence of the pressure source and increased viscous and cavitation-induced damping. From Fig. 13(b), it can be seen that compared with the inlet region, the tip clearance has more pronounced frequency-domain characteristics, due to the highly unsteady interaction between the leakage flow and the blade tip. Peak pulsating pressures occur at the blade frequency and its harmonics, with the most pronounced effect observed at gap P1 near the leading edge, indicating that the unsteady pressure field in the tip clearance is primarily driven by blade–vortex interaction and periodic blade loading. The largest amplitudes of the pressure fluctuations occur at position P1 near the leading edge of the blade, where the pressure gradient and leakage jet intensity are highest, favouring the formation of a coherent tip-leakage vortex. As the vortex moves downstream from P1 to P3, it undergoes diffusion and partial breakdown, resulting in a gradual decline in flow coherence and a shift in the dominating spectral energy from higher to lower frequencies.

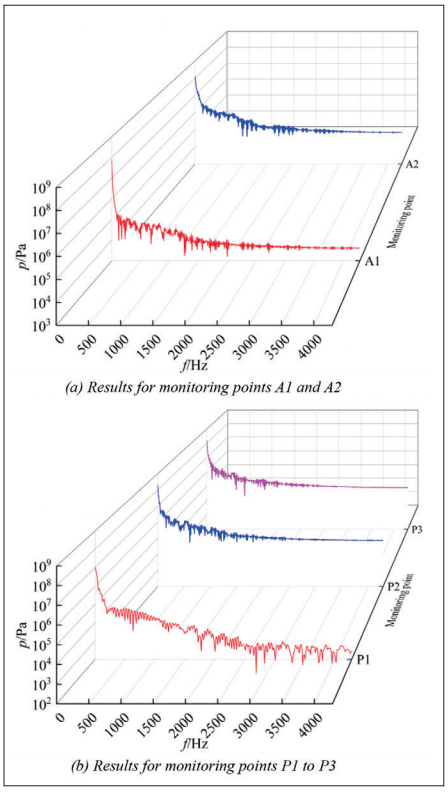

Fig. 13. Characteristics of the internal flow pulsation pressure for the IMP propulsor in the frequency domain

CHARACTERISTICS OF SOUND PRESSURE ATTENUATION

To monitor the far-field sound pressure of the IMP propulsor, we examined its attenuation characteristics in both the axial and radial directions. Five sound pressure monitoring points were established along the axial (A1–A5) and radial (R1–R5) directions of the IMP propulsor. The axial monitoring point A1 was located behind the centre of the IMP propulsor, and the radial monitoring point R1 directly above the centre. The spacing between adjacent monitoring points was constant. To analyse the sound pressure radiation patterns along the circumference of the IMP propulsor and their directionality, 24 monitoring points (C1–C24) were uniformly distributed counterclockwise around the centre of the IMP propulsor, with an angle of 15° between adjacent monitoring points. The arrangement of the sound pressure monitoring points is shown in Fig. 14.

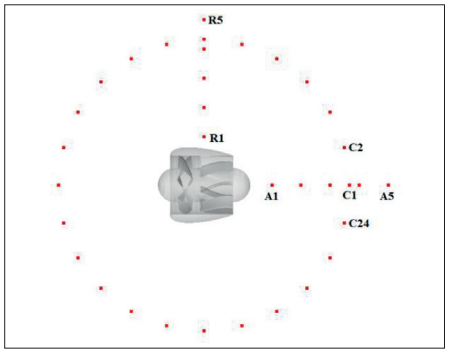

Fig. 14. Layout of the sound pressure monitoring points

The sound pressure level characteristics at the axial monitoring points (A1–A5) of the IMP propulsor in non-cavitation and cavitation states were compared (as shown in Fig. 15). The reference sound pressure for water as the fluid medium was selected as $2 \times 10^{-5} P_a$. It was found that the sound pressure level at the monitoring points decreased with increasing axial distance, with a distinct attenuation characteristic in both states. The noise energy from the IMP propulsor was primarily concentrated in the low-frequency range, with the sound pressure level gradually decreasing as the frequency increased. This pattern can be explained by the fact that higher-frequency acoustic components encounter greater viscous dissipation and dispersion, resulting in a smaller attenuation gradient with distance, while low-frequency acoustic components have longer wavelengths and travel more effectively in water.

By comparing the amplitude curves of the sound pressure level (see Fig. 16) at the axial monitoring points of the IMP propulsor in both the non-cavitation and cavitation states, it can be seen that the peak values at the blade passing frequency decrease as the distance increases. Furthermore, at equivalent frequencies, the sound pressure amplitude in the cavitation state exceeds that in the non-cavitation state. Taken together with Fig. 17, the main causes of the increased cavitation noise can be attributed to the conception, oscillation, and collapse of vapor bubbles, which cause significant unsteady pressure variations in the flow field. Cavitation shedding and tip-vortex cavitation augment the tonal components at the blade passing frequency and its

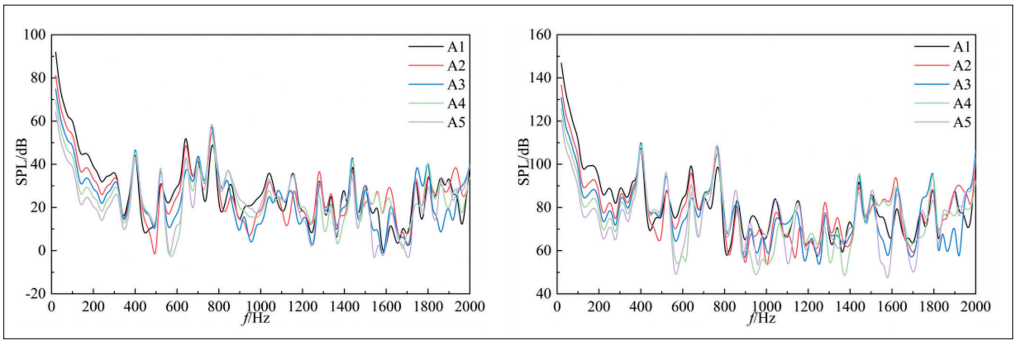

Fig. 15. Comparison of the sound pressure level at the axial monitoring points (A1–A5) of the IMP propulsor without cavitation and in a cavitation state (left: without cavitation; right: with cavitation)

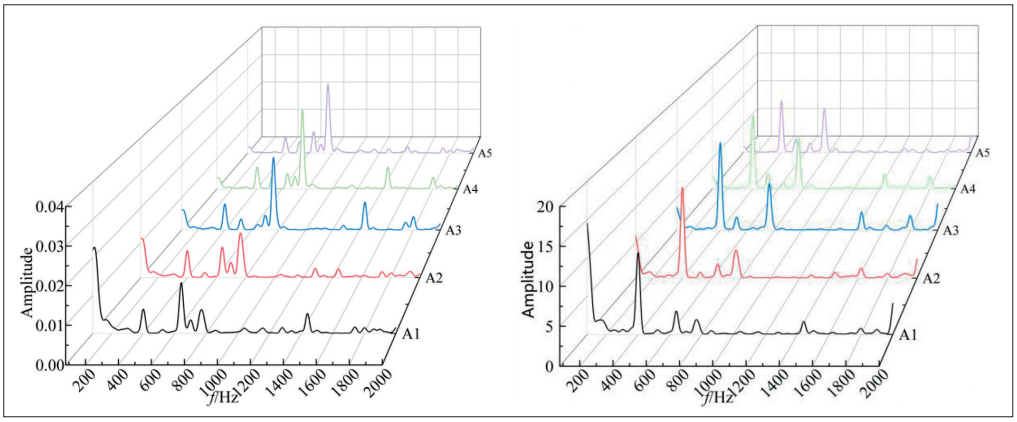

Fig. 16. Comparison of the sound pressure level amplitude (units: Pa) at the axial monitoring points (A1–A5) of the IMP propulsor without cavitation and in a cavitation state (left: without cavitation; right: with cavitation)

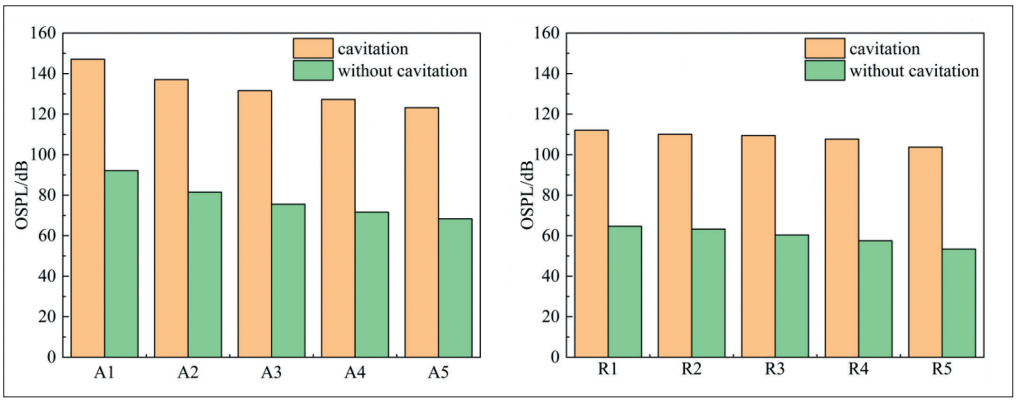

Fig. 17. Comparison of overall sound pressure levels at the pump-jet thruster monitoring points with and without cavitation (left: axial monitoring points (A1–A5); right: radial monitoring points (R1–R5))

harmonics, while the abrupt collapse of bubbles creates high-amplitude pressure pulses that result in broad-band noise. In addition, the cavitating region intensifies the radiated noise by acting as a dispersed and erratic acoustic source.

The sound pressure level curves of the IMP propulsor at the radial monitoring points were compared under cavitation and non-cavitation conditions (see Fig. 18). The findings demonstrated that as the distance of the radial monitoring points increased, the sound pressure level at the monitoring points also decreased. In comparison with the axial sound pressure monitoring points, the radial sound pressure does not demonstrate significant attenuation characteristics, with minimal variation in sound pressure levels at different positions, and a general decrease compared to the axial sound pressure levels. The presence of the duct structure is the reason for this phenomenon. The duct structure functions by reducing the pulsating pressure outside the duct, thereby lowering sound pressure levels in the external environment. The results for the radial monitoring points presented in Figs. 17 and 19 follow essentially the same pattern as for the axial direction.

To investigate the distribution features and directionality of the hydrodynamic noise from the IMP propulsor along the circular path in the mid-longitudinal plane, data from 24 circularly arranged monitoring locations were grouped and analysed. The overall sound pressure level at these 24 points (with adjacent monitoring points separated by 15°) were used to create a polar coordinate diagram to determine the directionality of the overall sound pressure level along the circumference of the IMP propulsor, as shown in Fig. 20.

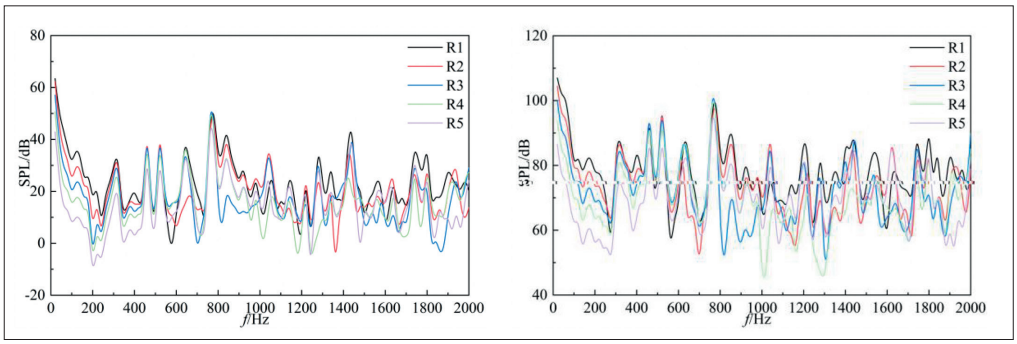

Fig. 18. Comparison of sound pressure levels at the radial monitoring points (R1–R5) of the IMP propulsor, without cavitation and in a cavitation state (left: without cavitation; right: with cavitation)

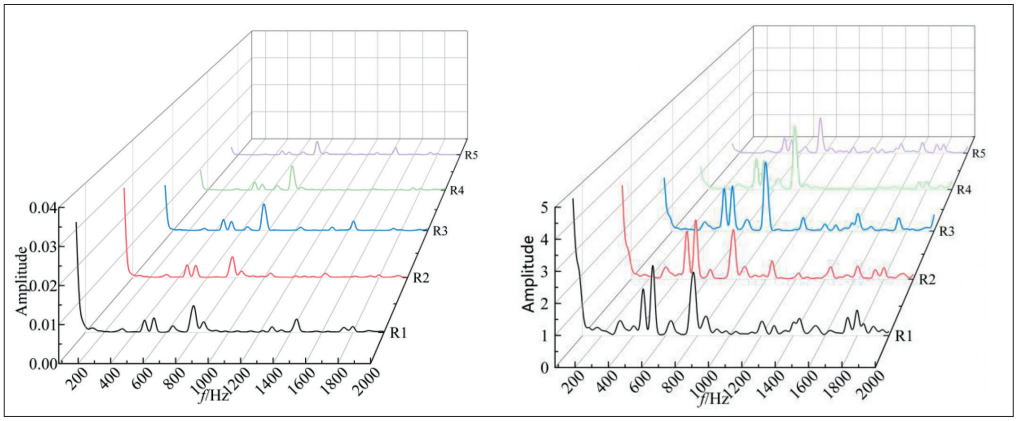

Fig. 19. Comparison of the sound pressure level amplitudes (units: Pa) at the radial monitoring points (R1–R5) of the IMP propulsor, without cavitation and in a cavitation state (left: without cavitation; right: with cavitation)

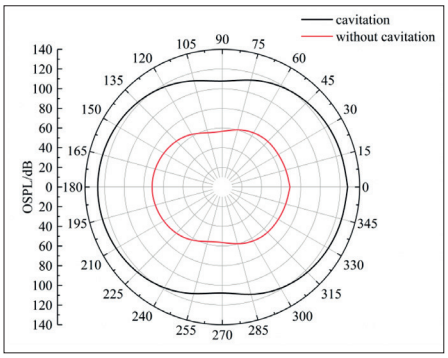

Fig. 20. Acoustic directivity of the IMP propulsor with and without cavitation

It was discovered that the overall sound pressure level of the IMP propulsor had monopole characteristics, with a lower overall sound pressure level at C7 (90°) and C19 (270°). This research revealed that the primary sound sources for the IMP propulsor are velocity and vortex volume. Given that all measurement locations in the radial plane are positioned at the same axial position, it is clear that the range of fluctuation in the total sound pressure level at each point is the same. As a result, the directivity pattern of the overall sound pressure level has an almost circular distribution. The overall sound pressure level is higher directly behind the IMP propulsor, meaning that the hydrodynamic noise of the propulsor has a considerable impact on the environment of the wake area adjacent to it.

To assess the impact of the cavitation noise on the surrounding environment, the noise reduction (NR) number was calculated for monitoring points A1–A5 and R1–R5 under cavitation conditions. The NR number is derived from a one-octave frequency spectrum, and incorporates both the intensity and frequency of noise within each frequency band. This metric is frequently used to assess the impact of noise on language, hearing impairment, and its effect on the surrounding environment, and is calculated with the following equation:

$$NR = \frac{L_p^i - a}{b} \tag{16}$$

where L_p^i is the sound pressure level value of the i-th one-octave frequency band, with units in *dB*; and a and b are constants related to the centre frequency of the one-octave frequency band. When the centre frequency is 1000 Hz, $a = 0$, $b = 1$.

Initially, we calculated the octave NR numbers for sound pressure reception points A1–A5 and R1–R5 from the octave frequency band (see Fig. 21). Following this, the maximum number of NR values for each centre frequency at each reception point were summarised in order to obtain the NR value for that specific point, as illustrated in Fig. 22.

As can be observed from Fig. 21, the sound pressure levels at various radial places are much lower than in the axial direction, indicating that the propulsor's cavitation noise is preferentially radiated into the downstream wake region. This effect is intimately related to the axial convection of cavitating tip vortices and vapor structures, which comprise the main sources of coherent noise. As shown in Fig. 22, the NR number for the axial monitoring points is reduced as the distance between the monitoring point and the propulsor rises, giving rise to a noticeable distance-dependent reduction of the transmitted noise in the downstream direction. This trend

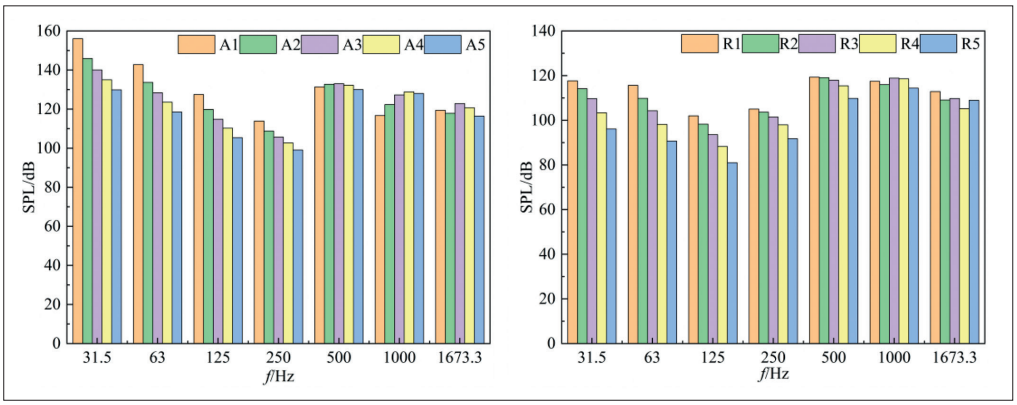

Fig. 21. Octave frequency band spectrum histograms (left: axial; right: radial)

implies that locations closer to the centre of the propulsor and the wake core are more heavily influenced by cavitation-induced hydrodynamic noise, which is dominated by coherent unsteady pressure sources along the axial flow direction. There is no substantial difference in NR counts between radial monitoring stations, suggesting that radial sound propagation is dominated by weaker and less coherent pressure fluctuations, resulting in a more uniform noise response in the radial direction compared to the prominent axial decay.

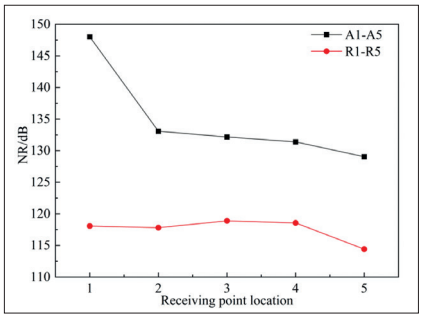

Fig. 22. NR curve at each monitoring point

ANALYSIS OF THE CAVITATION BUBBLE VOLUME PULSATION

Following the transient cavitation simulations, data representing the temporal evolution of cavitation bubble volume over three blade revolutions were extracted for different cavitation numbers. These data were then represented graphically and analysed.

In Fig. 23, the curves represent the variation in bubble volume due to pulsation at the blade, at different stages of cavitation. The mean bubble volume was determined to be 0.019 m^3 at the point of inception of cavitation. As the process of cavitation development progressed, there was a substantial increase in the average bubble volume, which reached 0.032 m^3. As the process progressed to the severe cavitation stage, an average increase in bubble volume was observed, reaching a value of 0.036 m^3. These findings suggest a positive correlation between the decrease in cavitation number and the increase in the average cavitation bubble volume within the blade. It can be concluded that as the severity of cavitation intensifies, the average cavitation bubble

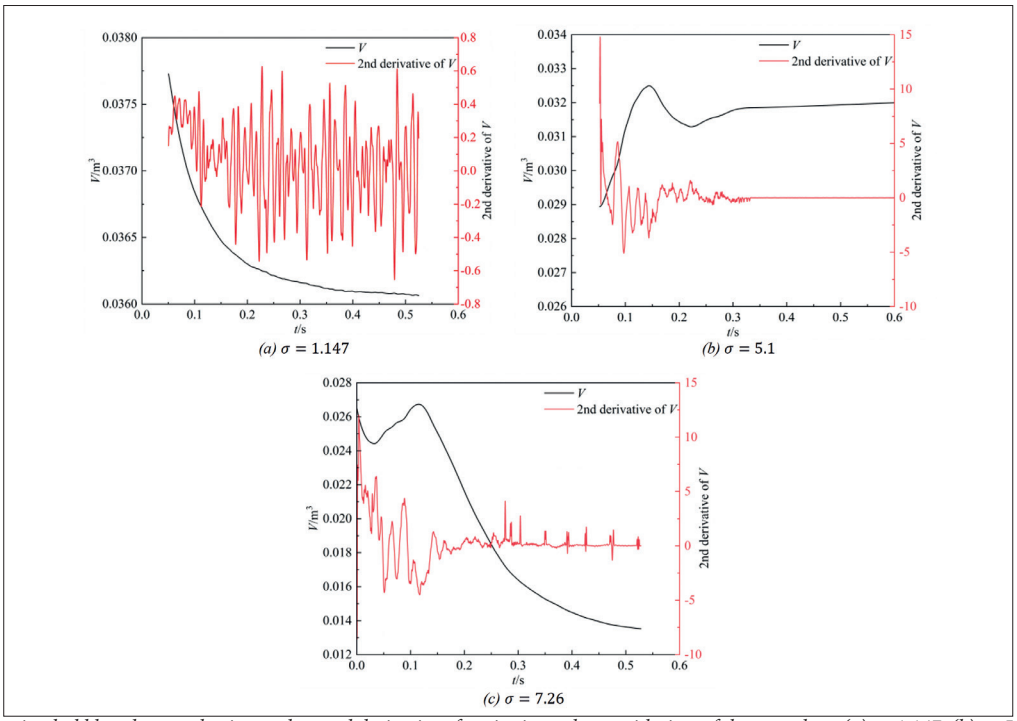

Fig. 23. Cavitation bubble volume pulsation and second derivative of cavitation volume with time of the propulsor: (a) σ=1.147, (b) σ=5.1, (c) σ=7.26

volume within the propulsor increases. Furthermore, an increase in pulsation amplitudes was observed in instances where reduced cavitation numbers were present, which could result in a decline in impeller pressure. It has been demonstrated that a lower pressure environment increases the likelihood of bubble collapse at locations that are farther from the centre of the propulsor. This, in turn, results in a higher average bubble volume within the propulsor. The decrease in pressure and the increase in instability provide favourable conditions for enhanced sound radiation.

ANALYSIS OF THE RADIATED NOISE CAUSED BY VOLUME PULSATION OF THE CAVITATION BUBBLE

In Fig. 24, spectrograms of the radiated noise from volume pulsation of the cavitation bubble in the propulsor are presented for varying monitoring points. The distance between the monitoring point and the noise source is shown to have no effect on the spectral characteristics of the radiated noise. Furthermore, it is found that the sound pressure level of the radiated noise decreases in proportion to the increase in distance between the monitoring point and the noise source.

Fig. 25 depicts the OSPL of the radiated noise at several monitoring stations. At the inception of cavitation ($\sigma = 7.26$), the OSPL at monitoring point A1 was 147.07 dB, while at point A2 it declined to 137.03 dB, and at point A5 it dropped further to 123.18 dB. At the stage of cavitation development ($\sigma = 5.1$), the OSPL at monitoring point A1 was 150.21 dB, which decreased to 148.47 dB at point A2, and declined further to 137.72 dB at point A5. At the severe cavitation stage ($\sigma = 1.147$), the OSPL at monitoring point A1 was 168.16 dB, decreasing to 161.44 dB at point A2 and again to 147.23 dB at point A5.

An investigation of the radiated noise spectra reveals that the SPL spectra for cavitation numbers 7.26, 5.1, and 1.147 show an initial fall followed by an increase. This observation implies that the energy is primarily concentrated in the low-frequency range, behaviour that is ascribed to large-scale unstable cavitation formations, whose growth and shedding cause significant low-frequency pressure variations. Under moderate cavitation circumstances, the periodic blade loading remains coherent, resulting in a significant increase in SPL at the blade passing frequency. As cavitation progresses to the severe regime (at a cavitation number of 1.147), massive vapour structures experience frequent shedding and collapse, with dramatically increasing wideband low-frequency noise. As a result, the OSPL rises, and significant peaks develop in the continuous frequency band between 100 and 300 Hz. In this domain, the dominance of cavitation-induced noise reduces the coherence of blade-passing-related pressure fluctuations, resulting in a lower SPL at the blade passing frequency.

Thus, within the same cavitation regime, the sound pressure level of the radiated noise drops as the distance between the monitoring point and the noise source increases, but the attenuation rate steadily decreases. This phenomenon is ascribed to acoustic attenuation and geometric spreading during sound propagation, as well as energy loss via scattering and absorption. As the propagation path length increases, acoustic energy gradually dissipates, and the radiated sound becomes more evenly distributed. As a result, monitoring stations farther from the noise source record lower sound pressure values. Meanwhile, as the propagation distance increases, the sound field becomes less coherent and spatially non-uniform, with a reduced distance-dependent attenuation gradient. As a result, the decay rate of radiated noise gradually reduces as the distance increases.

An investigation was conducted to ascertain the influence of the cavitation number on the radiation noise. Fig. 26 shows a spectrogram of the radiated noise at monitoring point A2. Across the different stages of cavitation, the sound pressure

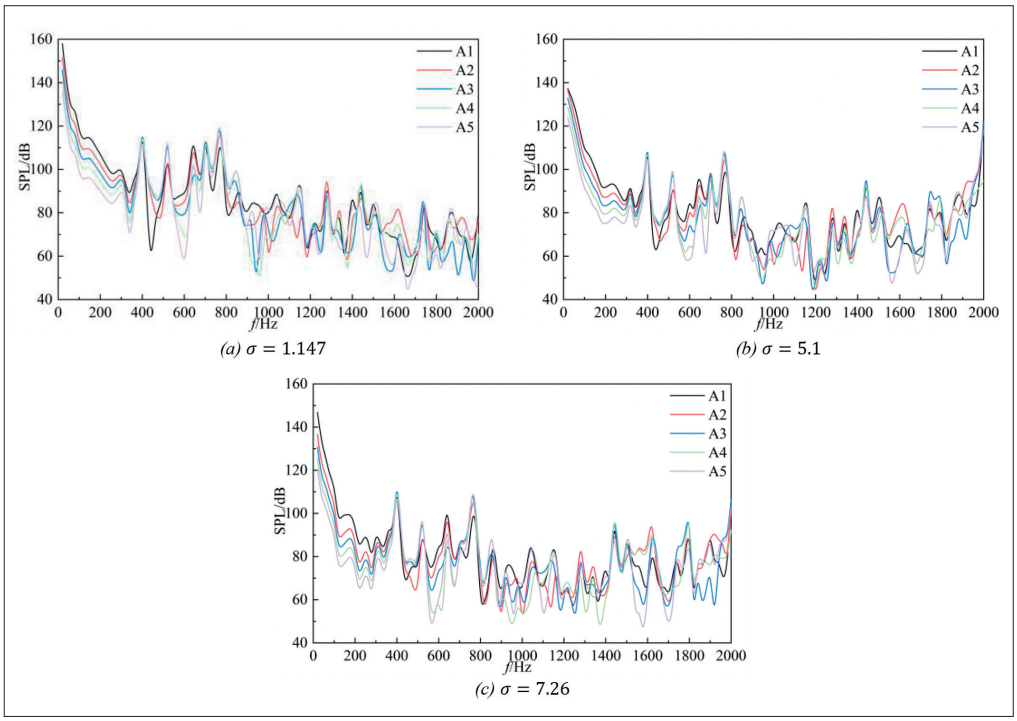

Fig. 24. Cavitation bubble volume pulsation of the propulsor: (a) σ=1.147, (b) σ=5.1, (c) σ=7.26

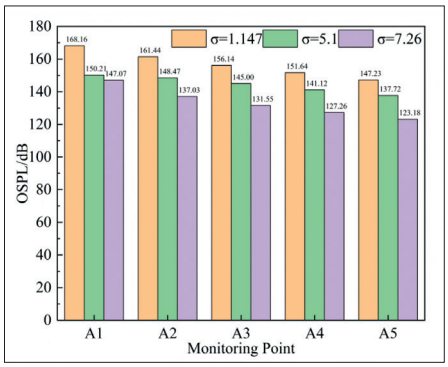

Fig. 25. Overall sound pressure level of the radiated noise at different monitoring points

level of the radiated noise from the propulsor initially decreases slightly and then gradually increases with increasing frequency. The spectral curves have the characteristics of a continuous spectrum. As the severity of cavitation increases, a general increase in the radiated noise is observed.

Furthermore, as can be seen in Fig. 26, the characteristic frequency of the radiated noise varies at different cavitation stages under constant conditions. This discrepancy may be attributed to variations in the pulsation amplitude of the bubble volume, the number of bubbles, and the velocity and pressure distributions in the flow field at stages of different cavitation. As cavitation progresses, the mechanisms of the major acoustic sources change from relatively coherent bubble oscillations to more complex processes that include cavity expansion, shedding, and collapse. These changes alter the acoustic interaction of sound waves with the cavitating medium, influencing the amount of reflection, scattering, and absorption during propagation. As a result, different cavitation regimes produce distinct frequencies that correspond to the maximum sound pressure level.

Fig. 25 shows that the OSPL of the radiated noise at point A2 undergoes a gradual increase as the cavitation number decreases. This phenomenon can be attributed to the intensification of cavitation, which has been shown to reduce pressure and increase the number of cavitation bubbles in the impeller. This, in turn, has been demonstrated to result in increased radiated noise.

CHARACTERISTICS OF THE CAVITATION NOISE WITH DIFFERENT GAPS

It is evident that alterations in the interstitial space significantly influence the flow characteristics of the vortex centre, consequently affecting the evolution of cavitation and noise in the flow field. In order to facilitate a more systematic analysis of the factors affecting cavitation and noise in the future, this section presents calculations of the cavitation flow under different gaps. It is hypothesised that this will facilitate the acquisition of a more comprehensive far-field noise characteristic for each operating condition, and that further comparison and analysis of the law governing these changes will be possible.

As illustrated in Fig. 27, the far-field OSPL under operating conditions 6, 3, and 2, which is demonstrated for different radial gaps referenced in the relevant literature [27]. It is evident that the size of the radial blade gap exerts a substantial influence on the intensity of cavitation noise. This is because changes in the gap alter the tip-leakage flow and the related tip-vortex cavitation dynamics. The OSPL directional distribution of the total cavitation noise under different radial gap conditions is closer to the characteristics of a monopole sound source when influenced by cavitation. This is because the intensity is the same in all directions. As the radial gap increases, the total noise initially decreases and subsequently increases, reaching a minimum when the radial gap condition is 3 mm.

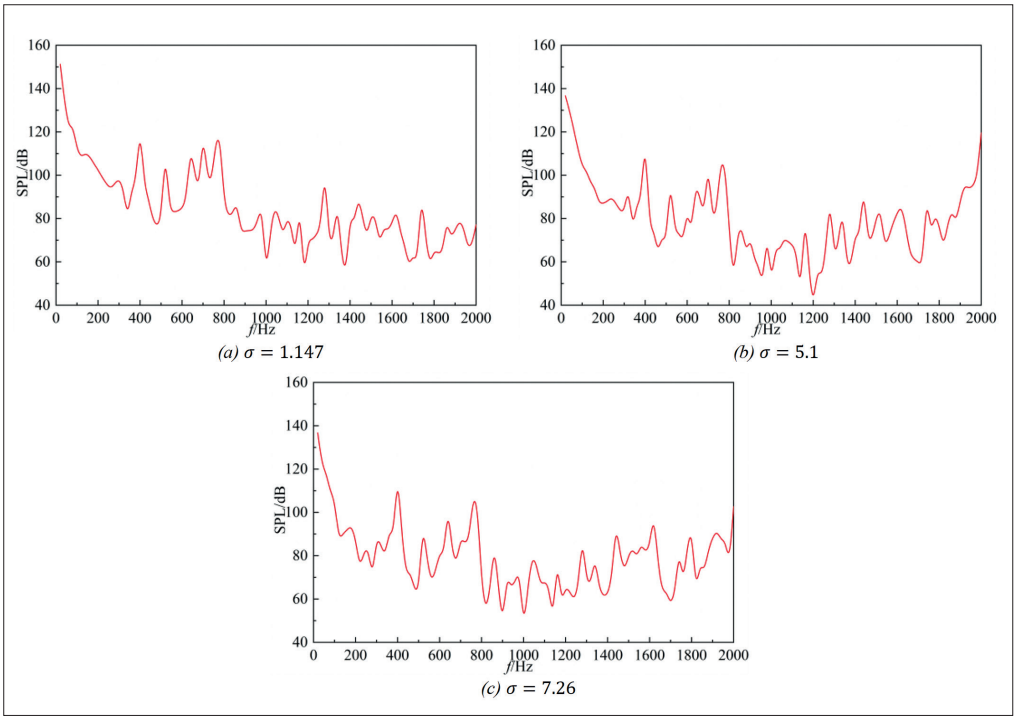

Fig. 26. Spectrograms of the radiated noise at monitoring point A2: (a) σ=1.147, (b) σ=5.1, (c) σ=7.26

The mesh resolution in the tip gap region was set following the strategy described in our previous studies [27], which has been shown to adequately resolve the gap flow structures.

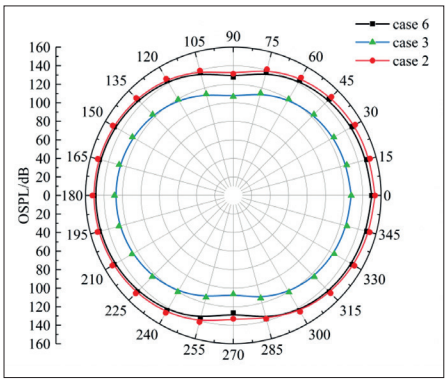

Fig. 27. Directivity diagram for the OSPL of cavitation flow noise under different radial gap conditions

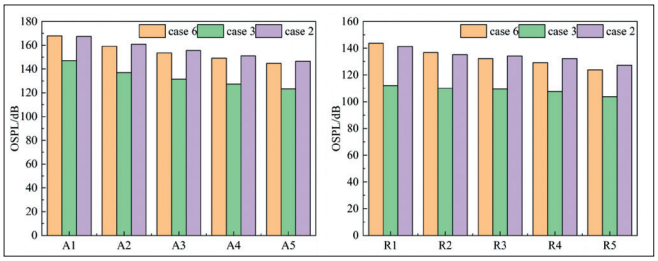

Fig. 28. Comparison of maximum OSPL values for cavitation flow noise under different radial gap conditions (left: axial; right: radial)

Fig. 28 shows a comparison between the OSPL results at the axial monitoring points A1–A5 and radial monitoring points R1–R5 under varying radial gap conditions. The OSPL shows a pattern of first decreasing and subsequently increasing as the clearance increases, reaching its minimum value at a radial gap size of 3 mm. Fig. 29 shows the spectral characteristics of cavitation flow noise, which can be observed to vary with differing radial gap conditions. The left-hand column displays the narrowband spectrum, while the right-hand column presents the one-third octave spectrum. It can be seen that the spectral characteristics of the noise across all frequency bands are consistent for different radial gaps, with a significant reduction at around 1000 Hz; this indicates that the dominant noise generation mechanisms remain unchanged, while the gap primarily modulates the noise intensity. The substantial decline at 1000 Hz may be due to the combined effects of lower acoustic source efficiency in this frequency range and increased attenuation of higher-frequency components during propagation. The intensity of the noise initially decreases and then increases as the radial gap is increased. Furthermore, high-frequency noise is typically lower than mid-to-low-frequency noise. As the radial gap increases, the noise intensity first drops, due to the weakening of concentrated tip-leakage vortices, and then increases as excessive leakage flow promotes unstable flow structures and cavitation. Cavitation-induced noise is dominated by low- and mid-frequency components associated with bubble volume oscillation and collapse, while high-frequency noise components are significantly reduced during transmission.

Fig. 30 presents the far-field OSPL under operating conditions 11, 10, and 9 under the various axial gaps described previously. It is evident that the size of the axial blade gap exerts a substantial influence on the intensity of cavitation noise. The OSPL directional distribution of the total cavitation noise under different axial gap conditions is found to be closer to the characteristics of a monopole sound source when influenced by cavitation, as evidenced by the intensity being the same in all directions. Based on the above analysis, the increase in the axial gap results in an increase in total noise. A wider axial gap expands the spatial scope of low-pressure regions and improves

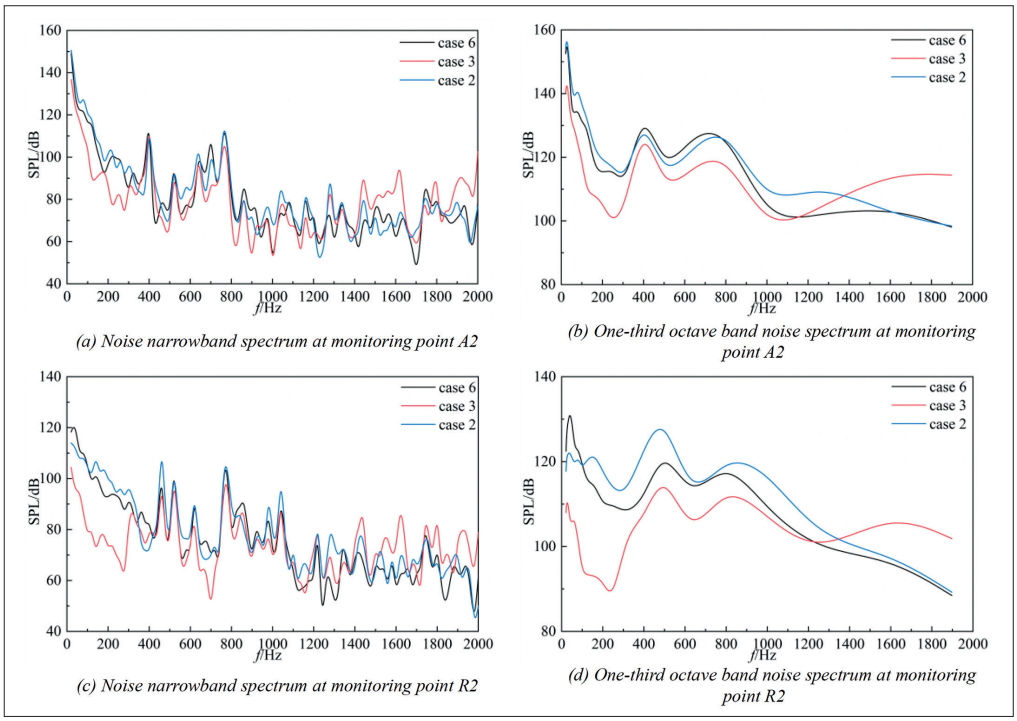

(a) Noise narrowband spectrum at monitoring point A2

(b) One-third octave band noise spectrum at monitoring point A2

(c) Noise narrowband spectrum at monitoring point R2

(d) One-third octave band noise spectrum at monitoring point R2

Fig. 29. Changes in the spectrum of cavitation flow noise with radial gap variation

unsteady flow interactions between the stator and rotor. This enhances cavitation formation and intensifies bubble oscillation and collapse, resulting in greater pressure fluctuations and overall noise radiation.

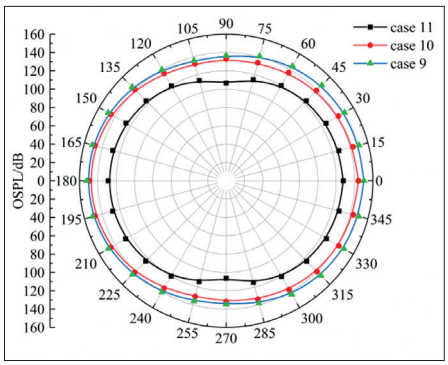

Fig. 30. Directivity diagram for the OSPL of cavitation flow noise under different axial gap conditions

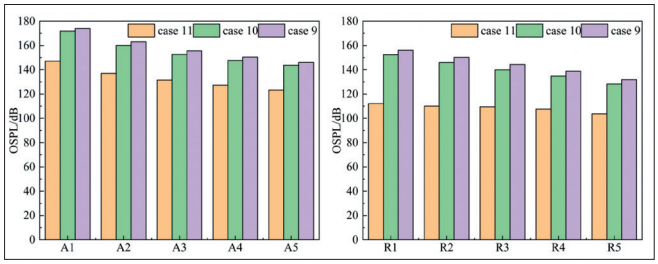

Fig. 31. Comparison of maximum OSPL values for cavitation flow noise under different axial gap conditions (left: axial; right: radial)

Fig. 31 presents a comparison of the OSPL results at axial monitoring points A1–A5 and radial monitoring points R1–R5 under varying axial gap conditions, which reveals a consistent increase in OSPL with increasing clearance, both axially and radially. Fig. 32 shows that the intensity of the noise increases in proportion to the axial gap.

In summary, at a given stage of cavitation, the OSPL of the radiated noise at a specific monitoring point increases with the axial gap. This phenomenon is likely to be attributable to an increase in the gap vortex, which has the potential to induce pressure pulsation and facilitate the radiation of low-frequency noise through the structure. Furthermore, the presence of a higher gap vortex engenders greater velocity gradients in the blade, thereby prompting more frequent movement and deformation of the cavitation bubbles and contributing to an increase in the radiated noise. This finding is aligned with the results reported in reference [27], which indicate that the vortex strength peaks at an axial gap of 6 mm.

CONCLUSION

In this study, we simulated and calculated the load noise characteristics of the E779A propeller model, and compared and verified the results against experimental data. The 'DES+FW-H' hybrid method was then employed to calculate the cavitation noise characteristics of the IMP propulsor, resulting in the following conclusions:

(1) The computational results for the E779A propeller load noise characteristics show a good degree of agreement with experimental data, providing proof of the dependability of the numerical calculation method described in this article.

(2) The hydrodynamic noise performance of the IMP propulsor is mostly concentrated in the low frequency range, regardless of whether cavitation is present. The noise shows clear attenuation characteristics in the axial direction of the IMP propulsor, but not in the radial direction. Furthermore, both have dipole features, and the OSPL at the axial position is low.

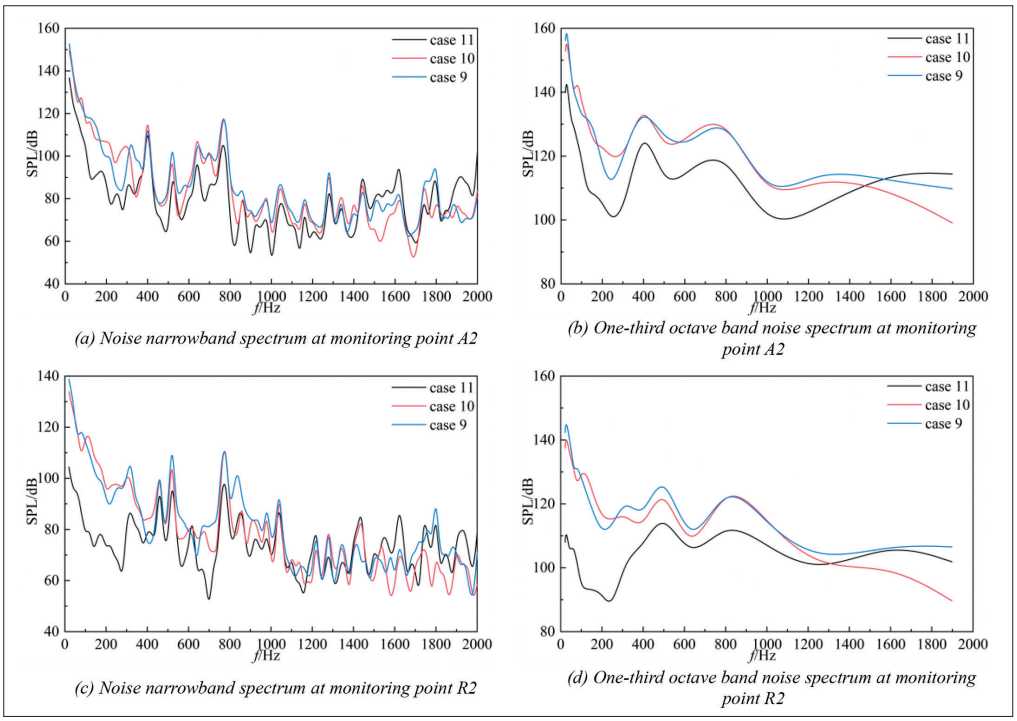

(a) Noise narrowband spectrum at monitoring point A2

(b) One-third octave band noise spectrum at monitoring point A2

(c) Noise narrowband spectrum at monitoring point R2

(d) One-third octave band noise spectrum at monitoring point R2

Fig. 32. Changes in the spectrum of cavitation flow noise with variation in the axial gap

(3) Cavitation causes the IMP propulsor to make more noise than under non-cavitation conditions. This increase in noise has been measured to be around 50 dB in terms of SPL. The rise in noise induced by cavitation in the IMP propulsor is rather consistent in all directions. The sound pressure level distribution in the radial direction does not exhibit attenuation properties, and the hydrodynamic noise from the IMP propulsor has a significantly smaller impact on the radial direction of the environment.
(4) An increase in cavitation intensity gives rise to an increased average bubble volume within the propulsor. It was also established that an increase in distance reduces the overall sound pressure level of radiated noise, and that the rate of this decline gradually decreases The sound pressure level spectra of the radiated noise in the propulsor exhibit continuous spectrum characteristics when the cavitation numbers are varied. It was also demonstrated that the overall sound pressure level of radiated noise increases as the cavitation number drops.
(5) Changing the blade tip gap significantly affects the level of cavitation noise. When the radial gap was set to 3 mm, the cavitation noise was reduced to its lowest level under the same axial gap conditions; in contrast, at a constant radial gap, increasing the axial gap caused an increase in cavitation noise, which can be attributed to enhanced vortex structures inside the flow field.

ACKNOWLEDGEMENTS

The authors would like to thank the Project of Young Innovative Talents in General Universities of Guangdong Province (Natural Science Category) (2023KQNCX114) and the department of Intelligent Manufacturing at Guangdong Technology College for their support for this research.

NOMENCLATURE

σ – cavitation number
p_{out} – outlet pressure
v – incoming velocity
k – turbulent kinetic energy
ω – specific dissipation rate
l_{DES} – turbulence length scale
Δ – local grid spacing
m_B – bubble mass
V_B – bubble volume
ρ_v – gas phase density
ρ_l – liquid density
p_v – evaporation pressure of the liquid at the local temperature
p – liquid pressure around the bubble
α_v – volume fraction of the gas phase
N_B – number of bubbles per unit volume
R_B – bubble radius
m_t – total mass transfer rate
R_e – vapor production rate
r – observation distance
V – volume of the cavitation bubble
$Q(t)$ – monopole source strength associated with temporal variation in the cavitation volume
u_i – components of fluid velocity
v_i – components of surface velocity
u_n – components of fluid velocity
v_n – components of surface velocity
$\delta(f)$ – Dirac delta function
$H(f)$ – Heaviside function
p' – acoustic pressure fluctuation
c_∞ – ambient speed of sound
T_{ij} – Lighthill stress tensor
σ_{ij} – viscous stress tensor
p'_T – thickness noise
p'_L – loading noise
U_n – normal velocity of the control surface
L_r – surface loading in the radiation direction
M_r – radiation Mach number
ret – delay time calculation integral

REFERENCES

1. Yuan JP, Wang ZL, Wang LY, Chen Y, Zhou YK. Review on the propulsion performance and noise of pump-jet propellers [in Chinese]. Ship Science and Technology 2022, vol. 44, no. 6, pp. 1-7.

2. Li Q. Multi-grid technology fusion generation method of integrated motor pump-jet propulsor [in Chinese]. Ship Engineering 2022, vol. 44, no. 05, pp. 90-95+101.

3. Du TC, Wu JG, Han GZ, Chen Y, Zhang MG, Wu TL. An analysis of noise radiation characteristics of pump-jet propulsor with rear stator [in Chinese]. Journal of Harbin Engineering University 2024, vol. 46, no. 3, pp. 62-68.

4. Sun C, Yue QH, Wang WQ, Wang, C. Numerical simulation of noise characteristics of pump-jet in uniform flow [in Chinese]. Huazhong Univ. of Sci. & Tech. (Natural Science Edition) 2023, vol. 51, no. 12, pp. 130-136.

5. Liu HL, Guo CY, Wu XF, Tan MG, Zhao Y. Numerical simulation on flow-induced noise in a shaftless pump-jet propulsor [in Chinese]. Journal Of Drainage and Irrigation Machinery Engineering (JDIME) 2025, vol. 43, no. 2, pp. 109-115.

6. Qin DH, Guang P, Seongkyu L, Huang QG, Yao S. Underwater radiated noise reduction technology using sawtooth duct for pump-jet propulsor. Ocean Engineering 2019, vol. 188, p. 106228. https://doi.org/10.1016/j.oceaneng.2019.106228

7. Zhang MY, Wang YS, Lin RL, Jin SB. Low-noise optimization design of pump-jet [in Chinese]. Journal of Huazhong

University of Science and Technology (Natural Science Edition) 2019, vol. 47, no. 3, pp. 7-12.

8. Ianniello S, Muscari R, Di Mascio A. Ship underwater noise assessment by the acoustic analogy: Part II: Hydroacoustic analysis of a ship scaled model. Journal of Marine Science and Technology 2014, vol. 19, no. 1, pp. 52-74. https://doi.org/10.1007/s00773-013-0236-z

9. Nitzkorski Z, Mahesh K. A dynamic end cap technique for sound computation using the Ffowcs Williams and Hawkings equations. Physics of Fluids 2014, vol. 26, no. 11. p. 115101 https://doi.org/10.1063/1.4900876

10. Mathey F. Aerodynamic noise simulation of the flow past an airfoil trailing-edge using a hybrid zonal RANS-LES. Computers & Fluids 2008, vol. 37, no. 7, pp. 836-843. https://doi.org/10.1016/j.compfluid.2007.04.008

11. McCormick BW, Elsenhuth JJ. Design and performance of propellers and pump-jets for underwater propulsion. AIAA Journal 1963, vol. 1, 10, pp. 2348-2354. https://doi.org/10.2514/3.2065

12. Testa C, Ianniello S, Salvatore F, Gennaretti M. Numerical approaches for hydroacoustic analysis of marine propellers. Journal of Ship Research 2008, vol. 52, no. 01, pp. 57-70. https://doi.org/10.5957/jsr.2008.52.1.57

13. Si QR, Ali A, Liao M, Yuan JP, Gu YY, Yuan SQ, Bois G. Assessment of cavitation noise in a centrifugal pump using acoustic finite element method and spherical cavity radiation theory. Engineering Applications of Computational Fluid Mechanics 2023, vol. 17, no. 1, p. 2173302. https://doi.org/10.1080/19942060.2023.2173302

14. Wei A, Wang S, Gao X, Qiu L, Yu L, Zhang X. Investigation of unsteady cryogenic cavitating flow and induced noise around a three-dimensional hydrofoil. Physics of Fluids 2022, vol. 34, no. 4, p. 042120. https://doi.org/10.1063/5.0088092

15. Sakamoto N, Kamiirisa H. Prediction of near field propeller cavitation noise by viscous CFD with semiempirical approach and its validation in model and full scale. Ocean Engineering 2018, vol. 168, pp. 41-59. https://doi.org/10.1016/j.oceaneng.2018.08.061

16. Jeong SJ, Hong SY, Song JH, Kwon HW, Seol HS. Establishment of cavitation inception speed judgment criteria by cavitation noise analysis for underwater vehicles. Proceedings of the Institution of Mechanical Engineers, Part M: Journal of Engineering for the Maritime Environment 2021, vol. 235, no. 2, pp. 546-557. https://doi.org/10.1177/1475090220967511

17. Ku G, Cheong C, Seol H. Numerical investigation of tip-vortex cavitation noise of an elliptic wing using coupled Eulerian-Lagrangian approaches. Applied Sciences 2020, vol. 10, no. 17, p. 5897. https://doi.org/10.3390/app10175897

18. Park C, Seol H, Kim K, Seong W. A study on propeller noise source localization in a cavitation tunnel. Ocean Engineering 2009, vol. 36, no. 9-10, pp. 754-762. https://doi.org/10.1016/j.oceaneng.2009.04.005

19. Pennings P, Westerweel J, van Terwisga T. Cavitation tunnel analysis of radiated sound from the resonance of a propeller tip vortex cavity. International Journal of Multiphase Flow 2016, vol. 83, pp. 1-11. https://doi.org/10.1016/j.ijmultiphaseflow.2016.03.004

20. Bosschers J. An analytical and semi-empirical model for the viscous flow around a vortex cavity. International Journal of Multiphase Flow 2018, vol. 105, pp. 122-133. https://doi.org/10.1016/j.ijmultiphaseflow.2018.03.021

21. Li Q, Abdullah S, Rasani MRM. Design analysis and optimisation of an integrated motor pump-jet thruster with improved resistance to cavitation. Ships and Offshore Structures 2024, vol. 19, no. 8, pp. 1010-1027. https://doi.org/10.1080/17445302.2023.2225963

22. Ghasemian M, Nejat A. Aero-acoustics prediction of a vertical axis wind turbine using large eddy simulation and acoustic analogy. Energy 2015, vol. 88, pp. 711-717. https://doi.org/10.1016/j.energy.2015.05.098

23. Mohamed MH. Reduction of the generated aeroacoustics noise of a vertical axis wind turbine using CFD techniques. Energy 2016, vol. 96, pp. 531-544. https://doi.org/10.1016/j.energy.2015.12.100

24. Ffowcs Williams JE, Hawkings DL. Sound generation by turbulence and surfaces in arbitrary motion. Philosophical Transactions of the Royal Society of London. Series A, Mathematical and Physical Sciences 1969, vol. 264, no. 1151, pp. 321-342. https://doi.org/10.1098/rsta.1969.0031

25. Orselli R, Meneghini J, Saltara F. Two and three-dimensional simulation of sound generated by flow around a circular cylinder. 15th AIAA/CEAS Aeroacoustics Conference 2009, p. 3270. https://doi.org/10.2514/6.2009-3270

26. Fu J, Wang YS. Frequency-domain prediction of propeller loading noise based on point source model [in Chinese]. Journal of Huazhong University of Science and Technology (Natural Science Edition) 2014, vol. 42, no. 4, pp. 77-80.

27. Li Q, Abdullah S, Rasani MRM. Hydrodynamic performance of an integrated motor pump-jet thruster with gap flow effects. Journal of Marine Science and Technology 2024, vol. 29, no. 4, pp. 789-811. https://doi.org/10.1007/s00773-024-01019-x